nature materials

SUPPLEMENTARY INFORMATION

DOI: 10.1038/NMAT3184

# High Electrochemical Activity of the Oxide Phase in Model Ceria-Pt and Ceria-Ni Composite Anodes

William C. Chueh[1,†], Yong Hao[†], WooChul Jung, Sossina M. Haile

Materials Science, California Institute of Technology, Pasadena, California 91125 USA

[1]Present Address: Sandia National Laboratories, Livermore, California 94551 USA

[†] Equally contributing authors

## Physical & Chemical Characterizations

Crystallinity of the metal-free SDC thin films was characterized by X-ray diffractometry (Phillips MRD, Cu kα source, 45 kV, 40 mA). The microstructure of as-fabricated samples was examined using a Carl Zeiss LEO 1550VP scanning electron microscope and analyzed by Image-Pro Plus software (Media Cybernetics). JEOL JXA-8200 electron probe microanalyzer was used for quantitative chemical analysis, with $CePO_4$ and $SmPO_4$ serving as standards. Higher resolution imaging of defined cross-sectional regions was obtained by focused ion beam milling using a FEI dual beam Helios FIB in combination with *in situ* secondary electron detection. For even higher resolution imaging, diffraction, and local chemical analysis, FEI Tecnai F20 and F30 transmission electron microscopes (TEM), equipped with EDAX energy dispersive spectrometers (EDS), were employed. FEI dual beam Nova 600 focused-ion beam (FIB) was used to prepare a cross-section sample; W thin film was used to protect the sample during milling. For select specimens, two samples were glued together, thinned, dimpled, and milled with Ar ions. High resolution EDS was performed in the scanning TEM mode. Surface chemical composition was determined using a custom X-ray photoelectron spectroscopy (Al kα source) system equipped with a Physical Electronics 10-360 hemispherical electron energy analyzer, as well as using a Phi 680 Auger nanoprobe. Surface morphology was characterized using a Park Systems XE-70 atomic force microscope (AFM).

DOI: 10.1038/NMAT3184

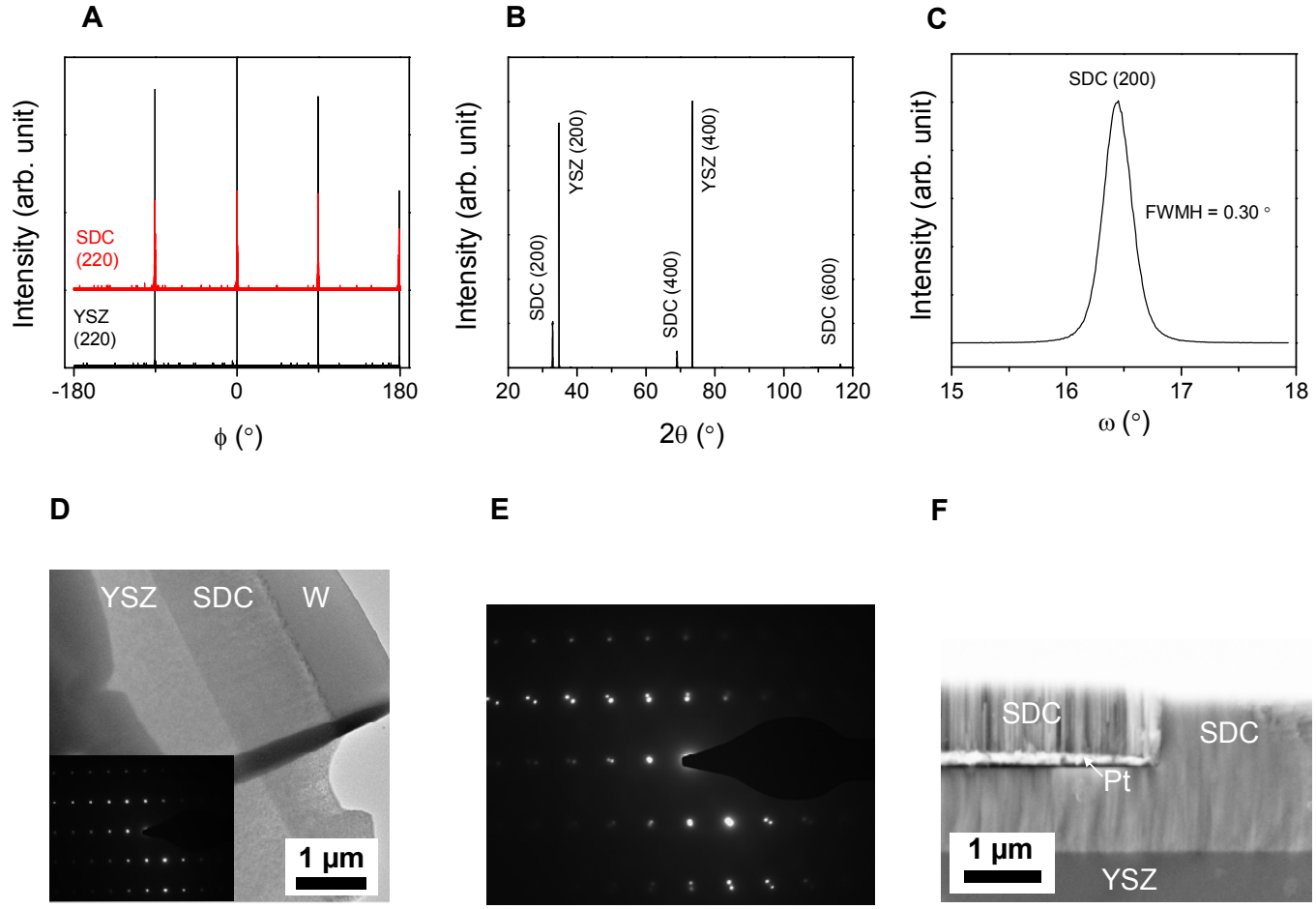


**Figure S1**: Physical characterizations of the SDC thin film. **(a)** In-plane, **(b)** out-of-plane and **(c)** rocking curve X-ray diffraction patterns for SDC thin film on YSZ(100) substrate. **(d)** Cross-sectional TEM image and selective area diffraction of SDC ((211) zone axis, inset) after annealing at 900 °C. **(e)** Selective area diffraction of the SDC-YSZ interface, (211) zone axis. **(f)** Cross-sectional SEM image of ceria-Pt-ceria cell with an embedded Pt current collector, after electrochemical characterization; apparent void between Pt and underlying SDC reflects slight damage during cross-section preparation.

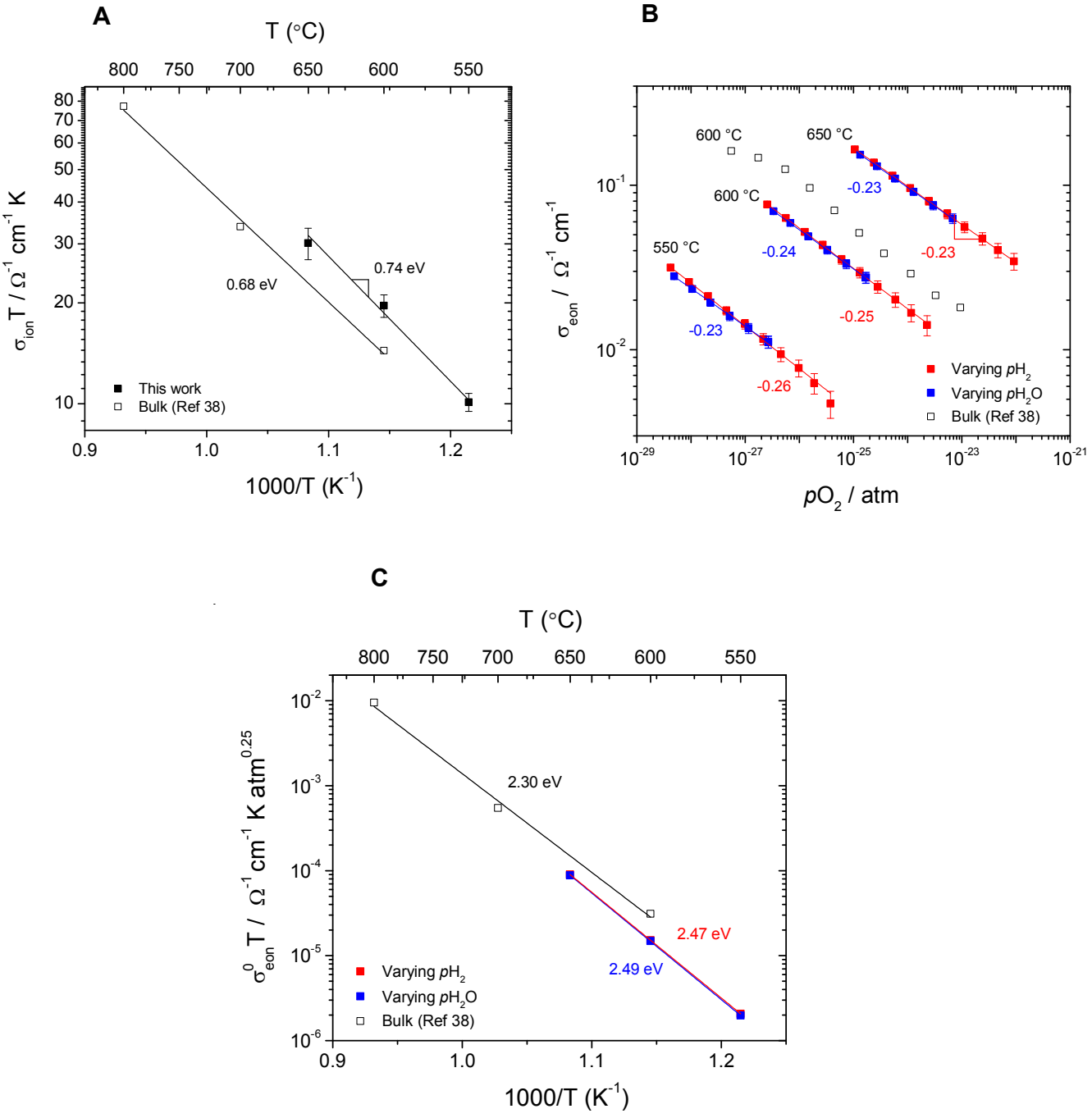


**Figure S2:** In-plane transport properties of 2.8 μm $Sm_{0.2}Ce_{0.8}O_{1.9-\delta}$ films grown on YSZ (100), with oxygen partial pressure varied by changing either hydrogen partial pressure or water vapor pressure. **(a)** Ionic conductivity (independent of gas phase atmosphere); (**b**) electronic conductivity; and **(c)** Arrhenius representations of $p_{O_2}$-independent term in electronic conductivity (obtained by fitting $\sigma_{eon} = \sigma^0_{eon} p_{O_2}^{-1/4}$ to data in

DOI: 10.1038/NMAT3184

**(b)**). In-plane conductivity was determined by taking the conductance difference between the YSZ substrate without and with the SDC thin film. Painted Pt strips applied to the edges of the samples served as electrodes and data were collected as a function of oxygen activity and temperature (550 to 650 °C). The substrate conductance accounted for 50 to 75% of the total, depending on the measurement conditions, implying a reliable conductance value for the film despite the tremendous difference in thickness of the two components (with errors not exceeding 19 %). Error bars calculated by assuming an error of 1 % on the measured resistance values for the YSZ substrate with and without SDC thin film.

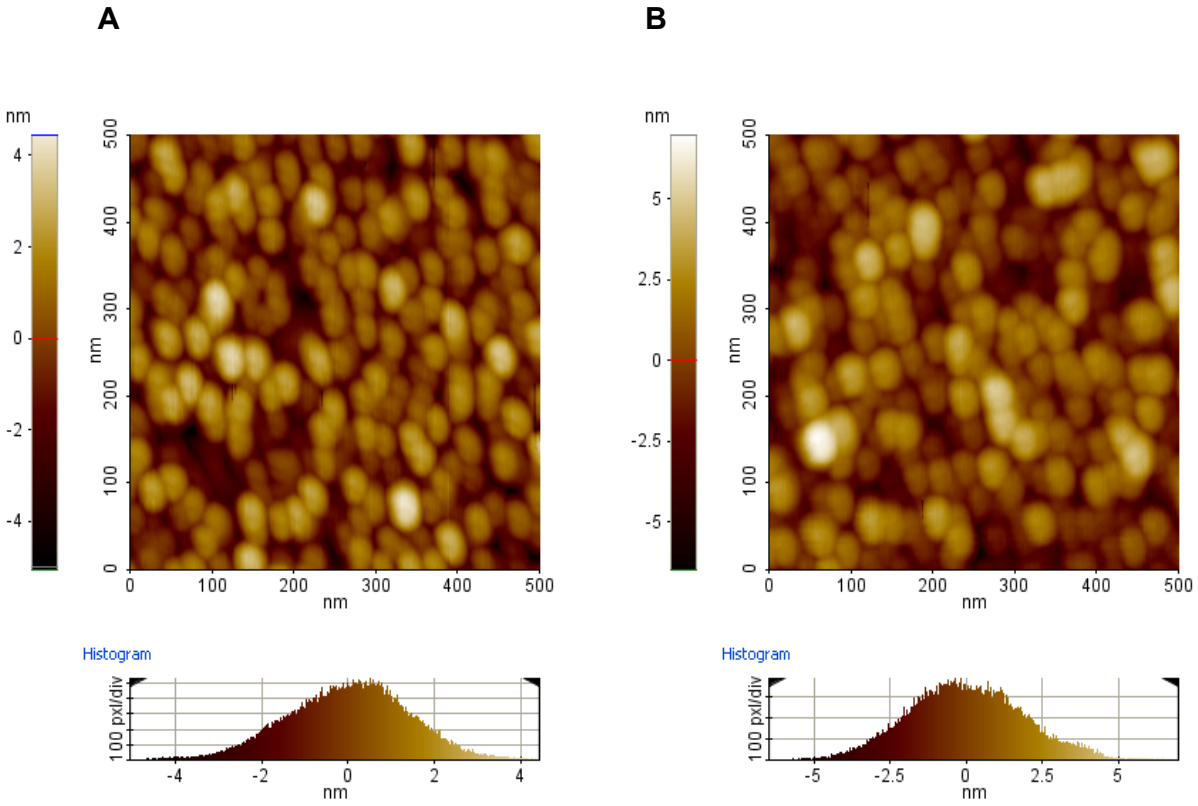


**Figure S3:** Non-contact AFM topography image of SDC thin film after electrochemical characterization in $H_2$-$H_2O$-Ar atmosphere at 650 °C. Region grown over **(a)** YSZ(100) and over **(b)** Pt on YSZ(100).

DOI: 10.1038/NMAT3184

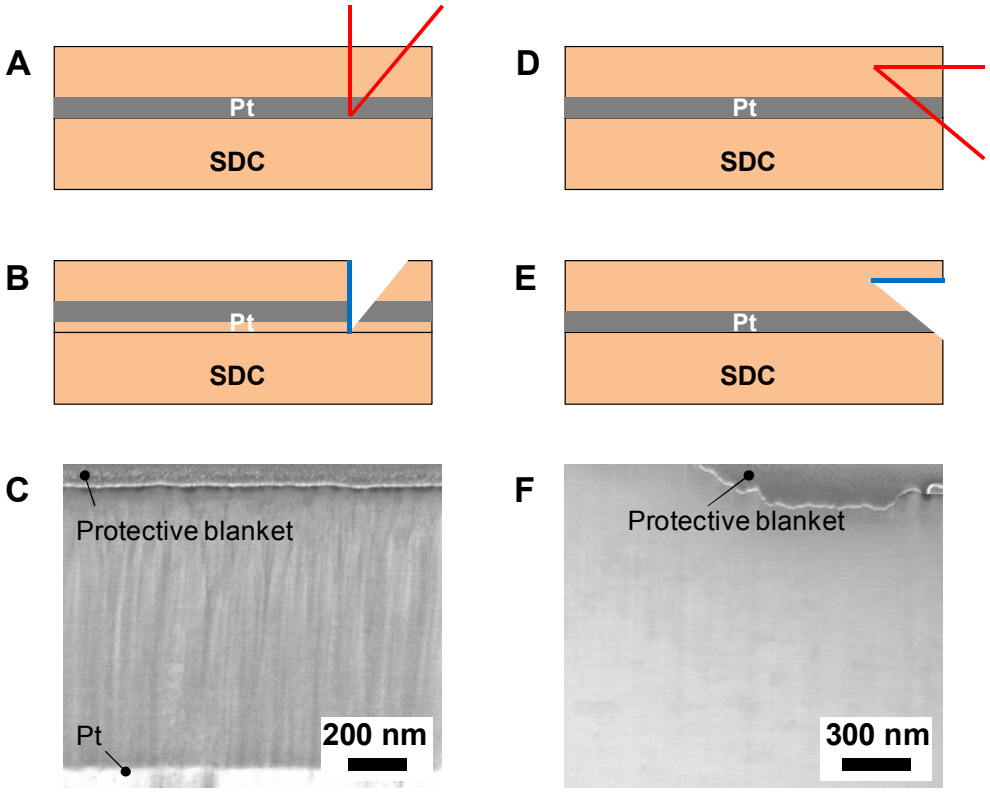


**Figure S4:** Scanning electron microscopy imaging of SDC grown over Pt; **(a)-(b)** and **(d)-(e)** showing focused ion beam milling of sample to obtain an image **(c)** normal to the film surface; and **(f)** parallel to the film surface. The surfaces imaged in **(c)** and **(f)** are highlighted in blue in **(b)** and **(e)**. The sample orientation depicted in **(a)-(b)** and **(d)-(e)** is rotated 90 ° about the surface normal axis from that in Figure 1.

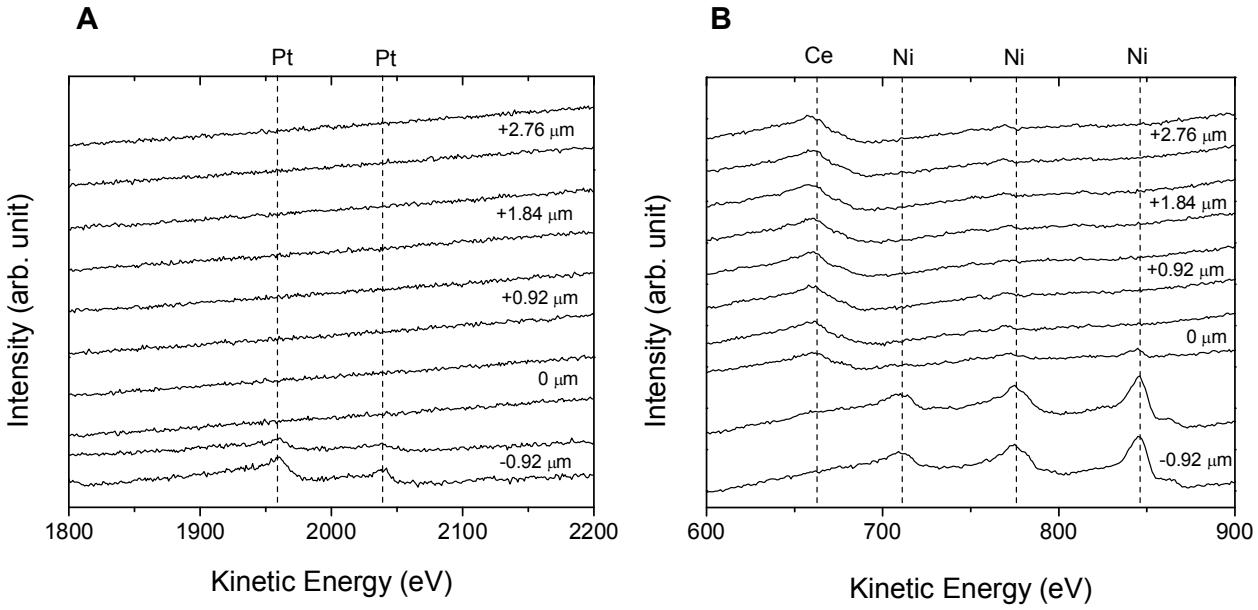


**Figure S5:** Auger electron spectroscopy line scans taken perpendicularly across the ceria-metal interface on the thin film surface, after electrochemical characterizations. Position indicates distance away from the interface, with positive values indicating the SDC side: **(a)** SDC-Pt and **(b)** SDC-Ni.

DOI: 10.1038/NMAT3184

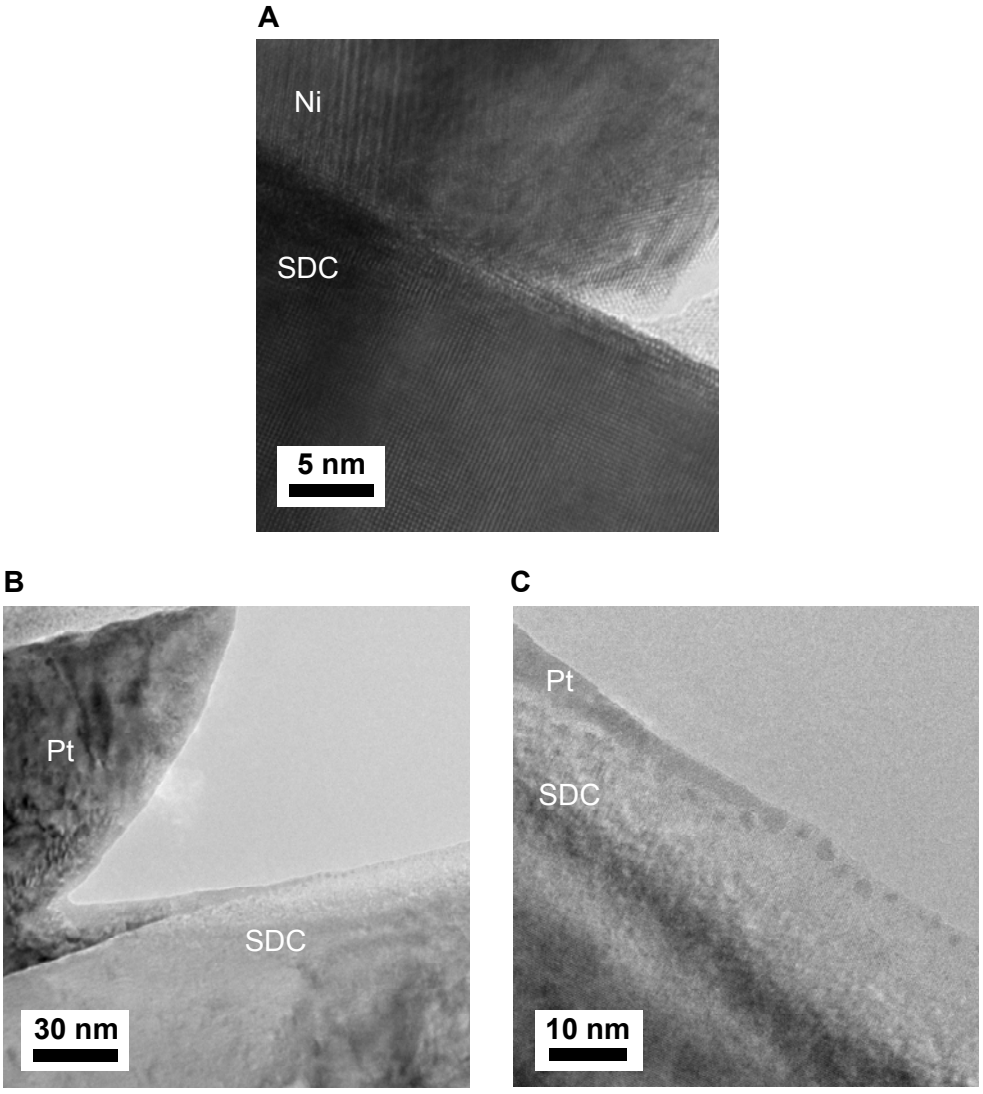


**Figure S6:** Cross-sectional TEM images of the triple-phase boundary in **(a)** SDC-Ni, and **(b,c)** SDC-Pt after electrochemical reaction.

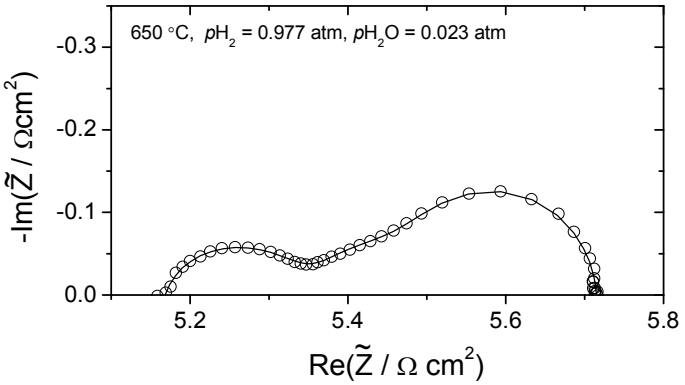


**Figure S7:** Impedance response of porous, columnar SDC symmetric cell with YSZ electrolyte. On the basis of the gas phase partial pressure dependence[1] and other evidences, the high frequency arc is preliminarily attributed to processes distinct from the surface electrochemical reaction.

DOI: 10.1038/NMAT3184

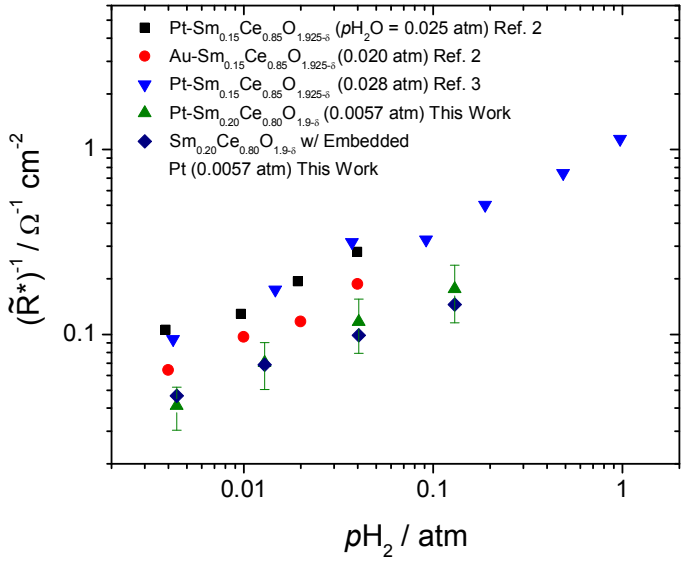


**Figure S8**: Comparison of electrode resistances of various Sm-doped cerias with normalization relative to the ceria active surface area (*i.e.*, metal coverage of some portion of ceria is accounted for) at 650 °C. The results obtained in this work using epitaxial SDC thin-film with patterned metal features (exposed Pt, averaged) agree qualitatively with the earlier results obtained using polycrystalline SDC with painted Au and Pt porous electrodes[2-4]. In the case of porous Pt, the relative reaction site density ($d_{3PB}$ to $d_{2PB}$ ratio) was approximately[4] $6 \times 10^3$ cm$^{-1}$, comparable to the highest relative reaction site density used in this work ($4.0 \times 10^3$ cm$^{-1}$) and justifying a direct comparison. The absolute surface reaction conductance values measured here agree, within an order of magnitude, with the earlier work. Differences in the absolute values are likely due to differences in the oxide surface structure; the present study employs a smooth, epitaxial thin film grown at ~ 650 °C, whereas the earlier work employed bulk-processed polycrystalline samples sintered at 1,350 °C. The higher activity of the polycrystalline material is plausibly due to higher roughness or the presence of high activity grain boundaries. Slightly differing measurement conditions (specifically gas atmospheres) were also employed.

**Table S1:** Nominal and actual line pattern dimensions and the corresponding reaction site densities.

| Metal | PLD Deposition Batch | Nominal Metal Line Width (µm) | Nominal Inter-metal Spacing (µm) | Nominal 3PB Density ($10^2$ cm$^{-1}$)* | Actual 3PB Density ($10^2$ cm$^{-1}$)* | Nominal 2PB Density | Actual 2PB Density |
|---|---|---|---|---|---|---|---|
| Pt | 1 | 5 | 5 | 20 | 21 | 0.50 | 0.61 |
| | 1 | 20 | 20 | 5.0 | 5.1 | 0.50 | 0.50 |
| | 1 | 40 | 40 | 2.5 | 2.5 | 0.50 | 0.50 |
| | 1 | 80 | 80 | 1.3 | 1.4 | 0.50 | 0.50 |
| | 2 | 40 | 120 | 1.3 | 2.3 | 0.75 | 0.75 |
| | 2 | 120 | 40 | 1.3 | 1.3 | 0.25 | 0.25 |
| | 2 | 150 | 10 | 1.3 | 1.3 | 0.06 | 0.06 |
| Ni | 3 | 5 | 5 | 20 | 22 | 0.50 | 0.56 |
| | 3 | 20 | 20 | 5.0 | 5.4 | 0.50 | 0.50 |
| | 3 | 40 | 40 | 2.5 | 2.8 | 0.50 | 0.52 |
| | 4 | 40 | 120 | 1.3 | 1.4 | 0.75 | 0.74 |
| | 4 | 120 | 40 | 1.3 | 1.4 | 0.25 | 0.24 |
| | 4 | 150 | 10 | 1.3 | 1.3 | 0.06 | 0.06 |
| Pt (Embedded) | 5 | 5 | 35 | 0.015 | 0.015 | 1.00 | 1.00 |

DOI: 10.1038/NMAT3184

**Table S2a:** Dependence of reaction rate on 3PB reaction site density.

| **Metal** | $p_{H_2}$ (atm) | $p_{H_2O}$ (atm) | $\frac{\Delta \log \tilde{R}^{-1}}{\Delta \log d_{3PB}}$ |
|---|---|---|---|
| Pt | 0.013 | 0.0058 | -0.09 ± 0.06 |
| | 0.013 | 0.0030 | -0.13 ± 0.06 |
| | 0.013 | 0.0015 | -0.15 ± 0.07 |
| | 0.013 | 0.00078 | -0.17 ± 0.07 |
| Pt | 0.13 | 0.0058 | -0.19 ± 0.02 |
| | 0.041 | 0.0058 | -0.17 ± 0.03 |
| | 0.013 | 0.0058 | -0.11 ± 0.06 |
| | 0.0044 | 0.0058 | -0.03 ± 0.08 |
| Ni | 0.016 | 0.0051 | 0.1 ± 0.3 |
| | 0.016 | 0.0026 | 0.2 ± 0.3 |
| | 0.016 | 0.0013 | 0.2 ± 0.3 |
| | 0.016 | 0.00065 | 0.2 ± 0.2 |
| Ni | 0.13 | 0.0052 | 0.0 ± 0.3 |
| | 0.041 | 0.0052 | 0.1 ± 0.3 |
| | 0.013 | 0.0052 | 0.2 ± 0.3 |
| | 0.0049 | 0.0052 | 0.2 ± 0.3 |

**Table S2b:** Dependence of reaction rate on 2PB reaction site density.

| **Metal** | $p_{H_2}$ (atm) | $p_{H_2O}$ (atm) | $\frac{\Delta \log \tilde{R}^{-1}}{\Delta \log d_{2PB}}$ |
|---|---|---|---|
| Pt | 0.013 | 0.0057 | 1.0 ± 0.3 |
| | 0.013 | 0.0029 | 1.0 ± 0.3 |
| | 0.013 | 0.0015 | 1.0 ± 0.3 |
| | 0.013 | 0.00076 | 1.1 ± 0.3 |
| Pt | 0.13 | 0.0057 | 1.2 ± 0.3 |
| | 0.041 | 0.0057 | 1.1 ± 0.3 |
| | 0.013 | 0.0057 | 1.0 ± 0.3 |
| | 0.0044 | 0.0057 | 0.9 ± 0.3 |
| Ni | 0.016 | 0.0057 | 1.2 ± 0.3 |
| | 0.016 | 0.0029 | 1.2 ± 0.3 |
| | 0.016 | 0.0015 | 1.2 ± 0.3 |
| | 0.016 | 0.00076 | 1.2 ± 0.2 |
| Ni | 0.13 | 0.0057 | 1.4 ± 0.3 |
| | 0.041 | 0.0057 | 1.3 ± 0.3 |
| | 0.013 | 0.0057 | 1.1 ± 0.2 |
| | 0.0049 | 0.0057 | 1.0 ± 0.1 |

**Supplementary References**

1 Brown, E. C. *Electrochemically deposited ceria structures for advanced solid oxide fuel cells* Ph.D thesis, California Institute of Technology, (2011).

2 Chueh, W. C., Lai, W. & Haile, S. M. Electrochemical behavior of ceria with selected metal electrodes. *Solid State Ionics* **179**, 1036-1041 (2008).

3 Lai, W. & Haile, S. M. Impedance Spectroscopy as a Tool for Chemical and Electrochemical Analysis of Mixed Conductors: A Case Study of Ceria. *J. Am. Ceram. Soc.* **88**, 2979-2997 (2005).

4 Ciucci, F., Chueh, W. C., Goodwin, D. G. & Haile, S. M. Surface reaction and transport in mixed conductors with electrochemically-active surfaces: a 2-D numerical study of ceria. *Phys. Chem. Chem. Phys.* **13**, 2121-2135 (2011).